JOURNAL OF PROPULSION AND POWER
Vol. 27, No. 1, January–February 2011

Time-Dependent Erosion of Ion Optics

Richard E. Wirz*
University of California, Los Angeles, Los Angeles, California 90095
and
John R. Anderson† and Ira Katz‡
Jet Propulsion Laboratory, California Institute of Technology, Pasadena, California 91001

DOI: 10.2514/1.46845

The accurate prediction of ion thruster life requires time-dependent erosion estimates for the ion optics assembly. Such information is critical to end-of-life mechanisms such as electron backstreaming. A two-dimensional ion optics code, CEX2D, was recently modified to handle time-dependent erosion, double ions, and multiple throttle conditions in a single run. The modified code is called CEX2D-t. Comparisons of CEX2D-t results with the NASA solar electric propulsion technology application readiness (NSTAR) thruster life demonstration test and extended life test results show good agreement for both screen and acceleration grid erosion, including important erosion features such as chamfering of the downstream end of the accelerator grid and reduced rate of accelerator grid aperture enlargement with time. The influence of double ions on grid erosion proved to be important for simulating the erosion observed during the NSTAR life demonstration test and extended life test.

Nomenclature

e	=	electron charge
J	=	ion current
j	=	ion current density
j^+	=	current density of singly charged ions
j^{++}	=	current density of doubly charged ions
KE	=	kinetic energy
n	=	number density
P	=	total thruster power
q	=	space charge density
v	=	velocity
Y	=	sputter yield
Γ	=	number flux
γ	=	double ion ratio j^{++}/j^+
σ	=	collision cross section

Subscripts and Superscripts

CEX	=	charge exchange
CEX^+	=	singly ionized charge-exchange ion
CEX^{++}	=	doubly ionized charge-exchange ion
c	=	code variable
dc	=	discharge chamber
S	=	flux of sputtered material from the grid surface
Xe^+	=	singly ionized xenon
Xe^{2+}	=	doubly ionized xenon
$+$	=	singly ionized
$++$	=	doubly ionized

Presented as Paper 2008-4529 at the 44th AIAA/ASME/SAE/ASEE Joint Propulsion Conference and Exhibit, Hartford, CT, 21–23 July 2008; received 30 August 2009; revision received 8 September 2010; accepted for publication 15 September 2010.

*Assistant Professor, Mechanical and Aerospace Engineering, 420 Westwood Plaza, Eng. IV 46-147B; wirz@ucla.edu.
†Senior Engineer, Electric Propulsion Group.
‡Group Supervisor, Electric Propulsion Group.

I. Introduction

ION optics erosion is one of the most critical life-limiting mechanisms for ion thrusters. Significant erosion of the ion optics grids was observed during the life demonstration test (LDT) and the extended life test (ELT) of the NASA solar electric propulsion technology application readiness (NSTAR) thruster [1,2]. This erosion resulted in excessive electron backstreaming (EBS) at the highest throttle condition for the NSTAR thruster during the ELT. Recent investigations of electron backstreaming show that strict cylindrical erosion of the acceleration grid holes does not explain the increase in electron backstreaming [2,3]. It is apparent that chamfering of the downstream end of the acceleration grid holes contributed to the high rates of EBS later in the thruster's life. To capture the effects of hole chamfering and other grid erosion phenomena, a self-consistent method for estimating the time-dependent grid erosion is needed. The ultimate goal of the work presented herein is to develop a model that will provide eroded grid geometries for the EBS model discussed in [3] and other models to accurately predict long-term thruster performance and end-of-life (EOL) conditions. The objective of this effort is to demonstrate a two-dimensional (2-D) model that accurately treats the time-dependent erosion of ion thruster optics.

Previous authors have developed time-dependent ion optics erosion codes that have provided useful results for understanding the erosion and long-term performance of ion thruster grids [4–10]. In this study, we will extend this field by incorporating double ion effects, using recent sputter yield data, and comparing with detailed grid cross sections from two long-duration life tests.

II. Formulation and Inputs

A technique for estimating the time-dependent erosion of the ion optics was developed using the CEX2D ion optics code (see [11] for details on CEX2D). For clarity, this new version of the code is referred to as CEX2D-t. Previous to this study, CEX2D provided erosion rates for a predefined grid shape comprising simple geometric shapes. The code was modified to use the erosion rate information to reduce the mass represented by the nodes defining the grid until the node's mass was reduced to zero. Once a node's mass is eliminated, the geometry is modified accordingly, and the ion optics code is then rerun to redefine the local potentials in the computational domain to determine the new beamlet characteristics in light of the new geometry. The new beamlet characteristics are then used to recompute the grid erosion rates until another node is eliminated. The grid geometry and remaining mass at each node are stored at the end

of each iteration. This process is repeated until a predefined thruster operation time is reached. The user may define various operating conditions for a series of thruster operating times to simulate throttled operation, such as demonstrated in the ELT. As discussed next, the effects of double ions on space charge and sputter yield were added to CEX2D-t as well.

A. Double Ion Formulation

In this section, the double ion current ratio γ is used to correct the sputter yield and charge density values that contribute to plasma bombardment of the upstream face of the screen grid and direct impingement of other grid surfaces. Similarly, the erosion rate due to charge-exchange (CEX) ions is corrected for double ion content. The double ion current is also used to correct the space charge in Poisson's equation. To formulate a double ion correction in CEX2D-t, we rely on the fact that, in a steady-state potential without magnetic fields, single ions and double ions follow the same trajectories. The total ion current density is the sum of the single and double ion current densities (assuming no other ion species):

$$j = j^{+} + j^{++} = j^{+}(1+\gamma) \tag{1}$$

Therefore,

$$j^{+} = \frac{1}{(1+\gamma)} j \quad \text{and} \quad j^{++} = \frac{\gamma}{(1+\gamma)} j \tag{2}$$

For sputtering from direct impingement from ions originating in the discharge chamber, we need to determine the fluxes of single and double ions to the surface. For this, the current densities are related to the ion number fluxes by

$$j^{+} = e\Gamma^{+}, \qquad j^{++} = 2e\Gamma^{++} \tag{3}$$

such that

$$\Gamma^{+} = \frac{1}{(1+\gamma)} \frac{j}{e}, \qquad \Gamma^{++} = \frac{\gamma}{(1+\gamma)} \frac{j}{2e} \tag{4}$$

Therefore, the flux of the grid material due to the sputtering caused by the impact of discharge chamber ions with the grid surface, including the effects of double ions, is

$$\Gamma^{S}_{\mathrm{dc}} = Y(\mathrm{KE}^{+})\Gamma^{+} + Y(\mathrm{KE}^{++})\Gamma^{++} \tag{5}$$

Combining the previous relations yields Γ^{S}_{dc} in terms of the current density and the double-to-single ion current ratio:

$$\Gamma^{S}_{\mathrm{dc}} = \frac{j}{e(1+\gamma)} \left[Y(\mathrm{KE}^{+}) + Y(\mathrm{KE}^{++}) \frac{\gamma}{2} \right] \tag{6}$$

The change in sputter yield due to doubly charged CEX ions is computed by considering the xenon CEX cross sections given in [12]. The code determines the current of CEX ions generated in a computational region of volume V_{cell} in the beamlet,

$$J^{c}_{\mathrm{CEX}} = j n_0 \sigma^{\mathrm{Xe}^{+}}_{\mathrm{CEX}^{+}}(\mathrm{KE}^{+}) V_{\mathrm{cell}} \tag{7}$$

where $\sigma^{\mathrm{Xe}^{+}}_{\mathrm{CEX}^{+}}$ is the collision cross section for singly charged CEX ions created by singly charged beamlet ions, and j is the local ion current density. Since the potential field is constant for a given iteration, the contribution of CEX ion generation from a given region in the beamlet can be related to a number flux to a grid surface (or out of the domain), such that

$$e\Gamma^{c}_{\mathrm{CEX}} = j n_0 \sigma^{\mathrm{Xe}^{+}}_{\mathrm{CEX}^{+}}(\mathrm{KE}^{+}) V_{\mathrm{cell}} \tag{8}$$

To correct this expression for double ions, we consider that the number fluxes originating from a region in the beamlet for single and double ions are given by

$$\begin{aligned} e\Gamma^{+}_{\mathrm{CEX}} &= j^{+} n_0 \sigma^{\mathrm{Xe}^{+}}_{\mathrm{CEX}^{+}}(\mathrm{KE}^{+}) V_{\mathrm{cell}} \\ 2e\Gamma^{++}_{\mathrm{CEX}} &= j^{++} n_0 \sigma^{\mathrm{Xe}^{2+}}_{\mathrm{CEX}^{++}}(\mathrm{KE}^{++}) V_{\mathrm{cell}} \end{aligned} \tag{9}$$

where $\sigma^{\mathrm{Xe}^{2+}}_{\mathrm{CEX}^{++}}$ is the collision cross section for doubly charged CEX ions created by doubly charged beamlet ions. The cross sections given in [12] show that the CEX generation mechanisms from the preceding equations dominate CEX production for ion thruster plumes. For example, the cross section for singly charged CEX ions created by doubly charged beamlet ions, $\sigma^{\mathrm{Xe}^{2+}}_{\mathrm{CEX}^{+}}$, is over an order of magnitude smaller than $\sigma^{\mathrm{Xe}^{2+}}_{\mathrm{CEX}^{++}}$, which results in a negligible effect for $\gamma < 1$. Combining the previous equations gives

$$\Gamma^{+}_{\mathrm{CEX}} = \frac{1}{(1+\gamma)} \Gamma^{c}_{\mathrm{CEX}}, \qquad \Gamma^{++}_{\mathrm{CEX}} = \frac{\gamma}{(1+\gamma)} \frac{\Gamma^{c}_{\mathrm{CEX}}}{2} \frac{\sigma^{\mathrm{Xe}^{2+}}_{\mathrm{CEX}^{++}}(\mathrm{KE}^{++})}{\sigma^{\mathrm{Xe}^{+}}_{\mathrm{CEX}^{+}}(\mathrm{KE}^{+})} \tag{10}$$

The flux of sputtered grid material due to impacts by CEX ions at the grid surface is found from

$$\Gamma^{S}_{\mathrm{CEX}} = Y(\mathrm{KE}^{+}_{\mathrm{CEX}})\Gamma^{+}_{\mathrm{CEX}} + Y(\mathrm{KE}^{++}_{\mathrm{CEX}})\Gamma^{++}_{\mathrm{CEX}} \tag{11}$$

Therefore, solving for the CEX sputter yield gives

$$\Gamma^{S}_{\mathrm{CEX}} = \frac{\Gamma^{c}_{\mathrm{CEX}}}{(1+\gamma)} \left[Y(\mathrm{KE}^{+}_{\mathrm{CEX}}) + Y(\mathrm{KE}^{++}_{\mathrm{CEX}}) \frac{\gamma}{2} \frac{\sigma^{\mathrm{Xe}^{2+}}_{\mathrm{CEX}^{++}}(\mathrm{KE}^{++})}{\sigma^{\mathrm{Xe}^{+}}_{\mathrm{CEX}^{+}}(\mathrm{KE}^{+})} \right] \tag{12}$$

The space charge density is computed by adding the charge densities of single and double ions for a given double ion current ratio. Initially, when calculating the charge density q_c, the code assumes all ions are singly charged. To correct for double ions, the higher velocity of the double ions accelerated through the same potential field must be considered. Therefore, the double ion correction for charge density for use in Poisson's equation is

$$q = \frac{1 + (\gamma/\sqrt{2})}{1+\gamma} q^{c} \tag{13}$$

B. Sputter Yield

The NSTAR ion thruster uses xenon propellant and molybdenum ion optics grids. The sputter yields for xenon on molybdenum for normal incidence used in this effort were taken from [13,14]. Yield curves were fitted to Stuart and Wehner's data [14] for $\mathrm{Xe}^{+} \rightarrow \mathrm{Mo}$ incidence energies above 140 eV, while Doerner et al.'s spectroscopic yield data [13] were used for incidence energies below 60 eV. Stuart and Wehner's [14] and Doerner et al.'s [13] data were linearly averaged for normal incidence between 60 and 140 eV. The sputter yields used herein represent the nominal yield data; future efforts will include sensitivity analysis to assess the impact of the uncertainty in the yield data. At this time, all ion impacts are assumed normal to the grid surface; future versions of the code will use the technique for accounting for offnormal incidence that is discussed in [11].

C. Thruster and Plasma Parameters

Posttest analysis of the NSTAR thrusters at the conclusion of the LDT and ELT tests showed that the center region of the grids experienced the most erosion and acceleration grid aperture enlargement, features which lead to increased EBS [3]. To simulate worst-case erosion, the code was run at center beamlet conditions for the full duration of the ELT using the thruster operating conditions shown in Table 1. The beamlet currents used in the analysis are shown in Fig. 1; these beamlet current profiles were calculated from LDT and ELT Faraday probe traces using the technique discussed in [2]. The neutral densities for TH12 and TH15 were taken as the average of the neutral densities from the exit plane neutral profiles in [15] and were scaled to the discharge flows rates for TH0, TH5, and TH8. The potential for the downstream beam plasma ϕ_{bp} and electron temperature T_e were taken as 15 and 1.8 eV, respectively, as discussed in [2]. The upstream electron temperature used was 5 eV, and the centerline double ion content estimates were taken from $E \times B$ data from the ELT and dawn preflight tests. The grid

Table 1 Input parameters for simulation of ELT

Test segment	Throttle level	J_b, A	P, kW	V_b	γ (center)	V_a	n_o (local)	End time, khr
1	TH12	1.49	1.96	1100	0.291	−180	7.30E + 17	0.447
2	TH15	1.76	2.33	1100	0.297	−180	7.50E + 17	4.693
3	TH8	1.1	1.46	1100	0.238	−180	3.88E + 17	10.451
4	TH15	1.76	2.33	1100	0.227	−260	5.67E + 17	15.617
5	TH0	0.51	0.52	650	0.061	−150	2.08E + 17	21.306
6	TH15	1.76	2.33	1100	0.262	−260	5.81E + 17	25.706
7	TH5	0.81	1.12	1100	0.197	−250	2.22E + 17	30.352

dimensions have been previously reported in several papers, including [16].

The nominal grid gap chosen for this analysis was the 0.30 mm spacing measured for TH15 in [17] (this assumes an initial cold grid gap of 0.66 mm and a lessening of the grid gap by 0.36 mm). However, the uncertainty in the change in grid gap measurement was ±0.073 mm, and the uncertainty in the measured cold grid gap was approximately ±0.015 mm. Reference [17] also showed that the grid gap change is likely closer to −0.02 mm for TH0 (−0.35 mm for TH8). Posttest analysis for the LDT and ELT showed that the cold grid gap had changed approximately −0.08 and −0.20 mm, respectively. From these data, it is clear that the grid gap measurement is highly uncertain and the grid gap value for a given throttle level may change during the test. At this time, the code does not allow for the grid gap to change during a given run; therefore, a range of constant grid gaps were used on several runs to assess erosion sensitivity to grid gap choice. The results from these runs are shown in the following section.

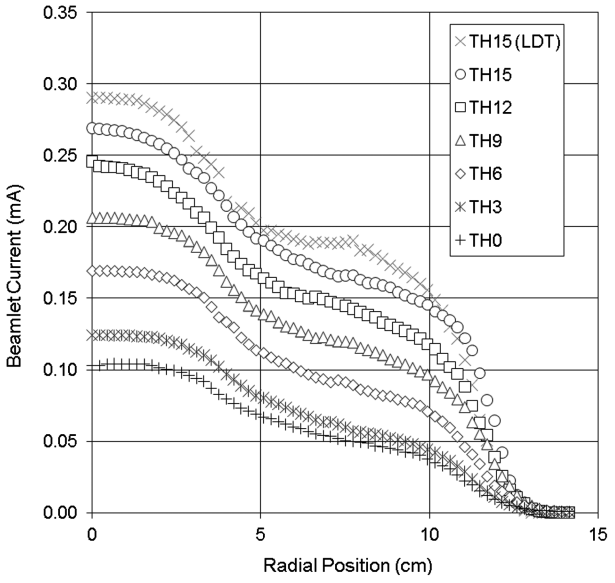

Fig. 1 Beamlet current vs radial position for ELT and LDT at TH15 for various throttle conditions.

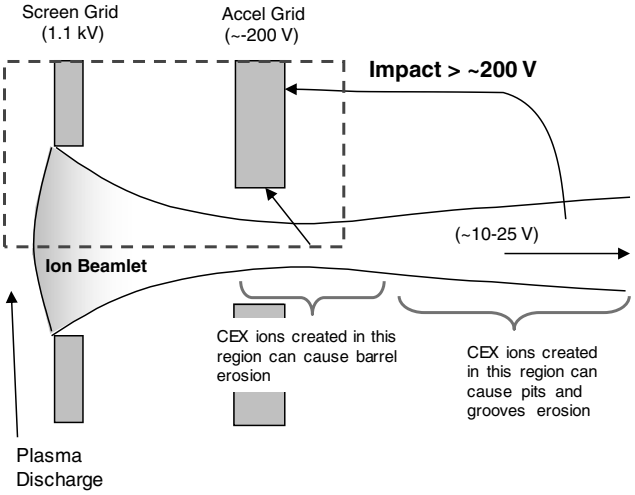

Fig. 2 Diagram of CEX erosion mechanisms for a single beamlet.

III. Analysis and Results

A simple parametric analysis of the previous equations provides an indication of the importance of considering double ions for grid erosion analysis. This analysis is not entirely self consistent, but it provides a means to interpret the erosion estimates made by CEX2D-t. The relative flux of sputtered material due to the impact of discharge ions of the upstream grid surface (using $\Gamma^S_{\rm dc}$) was analyzed assuming discharge ions hit the screen grid with energy equal to the discharge voltage; therefore, energy of 25 V was used for single ions. The sensitivity analysis for the flux of sputtered material due to the impact of CEX ions on the acceleration grid (using $\Gamma^S_{\rm CEX}$) was performed by assuming the singly charged ion energy was the beam plasma potential minus the acceleration grid potential (i.e., for single ions, the nominal case gives $\phi_{\rm bp} - V_a = 15 + 180 = 195$ V; worst case gives $\phi_{\rm bp} - V_a = 15 + 260 = 275$ V). A basic diagram of the grids and grid erosion mechanisms is shown in Fig. 2. The region of Fig. 2. surrounded by the dotted line is the portion of the computational domain that is used in later figures to show the grid erosion results from CEX2D-t (the entire computational domain extends 5 cm downstream). The results of this simple parametric analysis, normalized to the $\gamma = 0$ case, are shown in Fig. 3. These results show that an increased double ion ratio (which can be as high

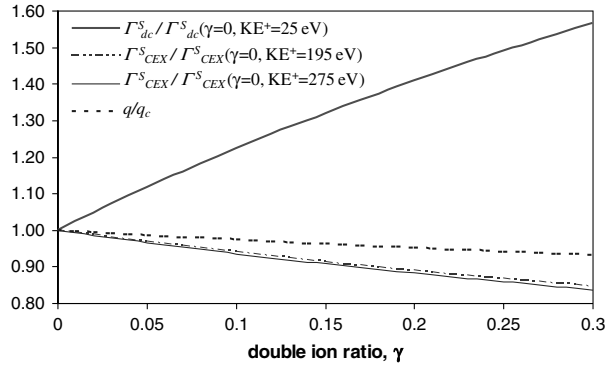

Fig. 3 Sensitivity analysis of surface flux of sputtered material and charge density vs double ion ratio.

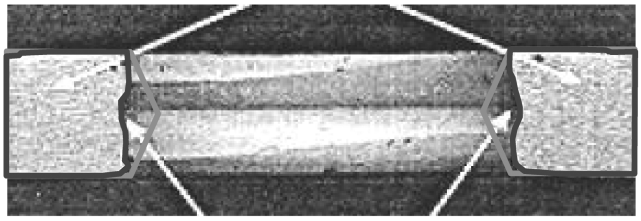

Fig. 4 Center-hole acceleration grid cross section after 8200 h LDT at TH15. (Original image from [1].)

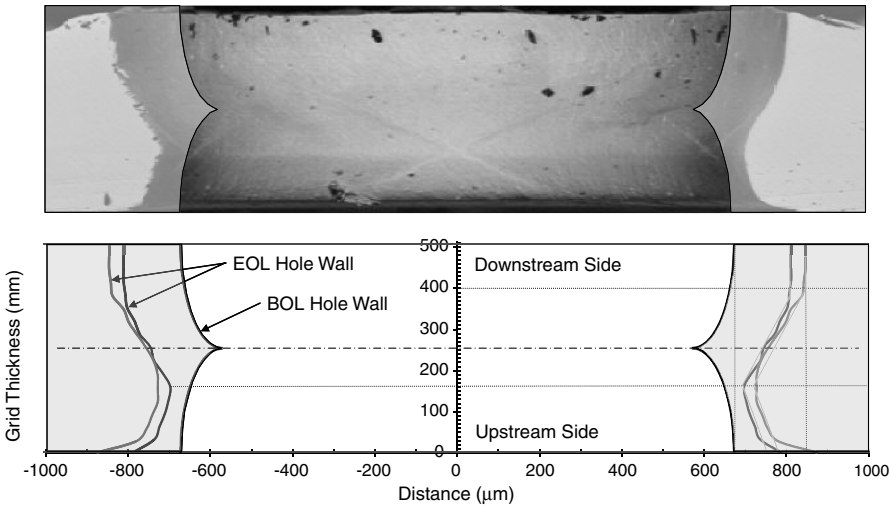

Fig. 5 Cross section of center-hole acceleration grid for ELT compared with approximate BOL geometry. The erosion pattern shows some departure from axisymmetry; therefore, two different ELT hole wall topographies are used for comparison with computational results in Figs. 6 and 8–10. (Original image from [2].)

as 0.3 for NSTAR on centerline) significantly increases the direct sputter yield for the screen grid. The acceleration grid erosion due to CEX ions decreases for increasing double ion content due to the fact that the effective number of ions is reduced by a factor of two and the yield at double ion energy is less than twice that for single ions at the energies of interest; in addition, at these energies, the ratio of the collision cross sections for doubly to singly charged CEX ions is less than half. The results also show that increased double ion content reduces charge density modestly, which is clear from the equation from the previous formulation.

To provide a comparison with the computational results, a cross section of the center hole on the acceleration grid for the LDT is shown in Fig. 4 at the conclusion of the 8200 h test. Comparison of the hole wall topography shows that the erosion is very nearly symmetric about the gridlet axis; therefore, an average hole wall topography for the LDT is used for comparison with computational results in Figs. 6 and 7. A cross section of the center-hole acceleration grid at the conclusion of the 30,352 h ELT is shown in Fig. 5. The erosion pattern is not axisymmetric; therefore, two different ELT hole wall topographies are used for comparison with the computational results in Figs. 6 and 8–10. These cross sections are used to compare to the acceleration grid erosion patterns determined by the code. For the screen grid erosion, we simply estimate a chamfered shape and screen grid thickness change from the LDT and ELT test data, as shown on the acceleration grid in Fig. 5. During the LDT, the upstream side of the screen grid chamfered at a depth of up to 40 μm and a width of up to 80 μm at the center hole, with an overall thickness reduction of up to $\sim$20 μm. The ELT experienced similar chamfering of the screen grid, and over 80 μm of the overall surface on upstream side of the screen grid was eroded away by the end of the test. Note the grid masses for each cell in Figs. 6–10 are weighted by the mass represented by that cell; therefore, the masses will be generally higher off axis. This is clearly evident from the radial dependence of the contour in Fig. 6. For the eroded shapes in Figs. 7–10, we see which nodes are losing mass by noting the cell color relative to cells at the same radial location. As noted earlier for Fig. 5, the aperture for the ELT shows asymmetric erosion; therefore, the grid topographies on both sides of the eroded aperture cross section are used to compare with the computational results discussed next.

Time-dependent screen and acceleration grid erosion profiles were determined for the NSTAR LDT and ELT using CEX2D-t and the parameters discussed previously and shown in Table 1. Center-hole erosion for the LDT was simulated by running the TH15 condition from test segment 2 of the ELT from 0 to 8200 h at a slightly higher beamlet current density to match the slightly higher centerline beam current, as shown in Fig. 1. The beginning-of-life (BOL) grid geometry and mesh are shown in Fig. 6. The erosion estimate by CEX2D-t for the 8200 h LDT, shown in Fig. 7, compares well to experimental profiles derived from LDT data. The disagreement related to erosion of the downstream end of the acceleration grid (commonly referred to as pits and grooves erosion) is expected, since the erosion in this region near the radial maximum of the domain is better treated by a three-dimensional (3-D) code, such as CEX3-D, due to the inherent 3-D nature of this region for the hexagonal geometry of the gridlet, as described in [18]. The code nearly predicts the magnitude of upstream screen grid erosion but does not clearly

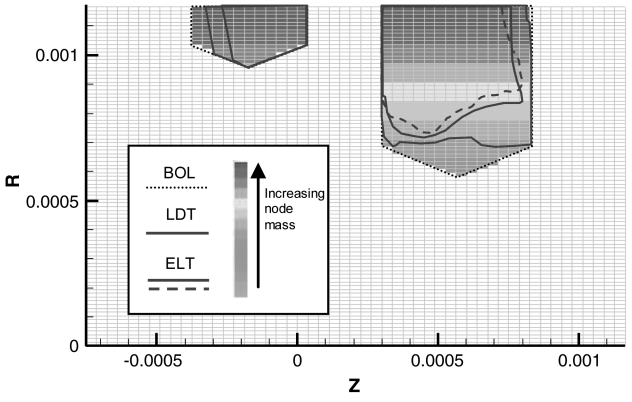

Fig. 6 BOL grid geometry at start of simulation. Computational grid in near field is shown; however, mesh extends 5 cm downstream to include downstream CEX ions that contribute to erosion.

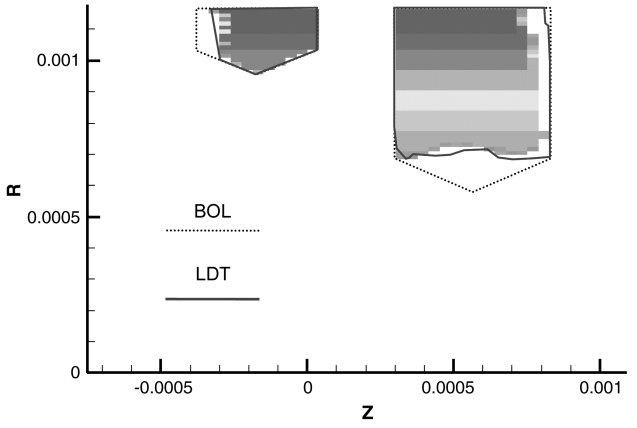

Fig. 7 LDT erosion estimate after 8200 h compared with experimental profiles.

demonstrate the chamfering of the screen grid as observed in posttest analyses; this may also be resolved by a 3-D treatment. Another consideration is to modify the velocity with which the ions are introduced from the upstream surface of the computational domain. At this time, the ions enter the domain with the Bohm velocity, which may be too high for the ions to be properly affected by potentials caused by the beamlet sheath.

The results for the predicted erosion profiles at the end of the seven test segments of the ELT are shown in Fig. 8. The expired times do not match the ELT exactly, since the code time steps are dictated by node losses; this inaccuracy is most notable for the end of test segment 5 where TH0 progresses for over 1400 h beyond the prescribed end time. These data show the following behavior assumed by Brophy [2]:

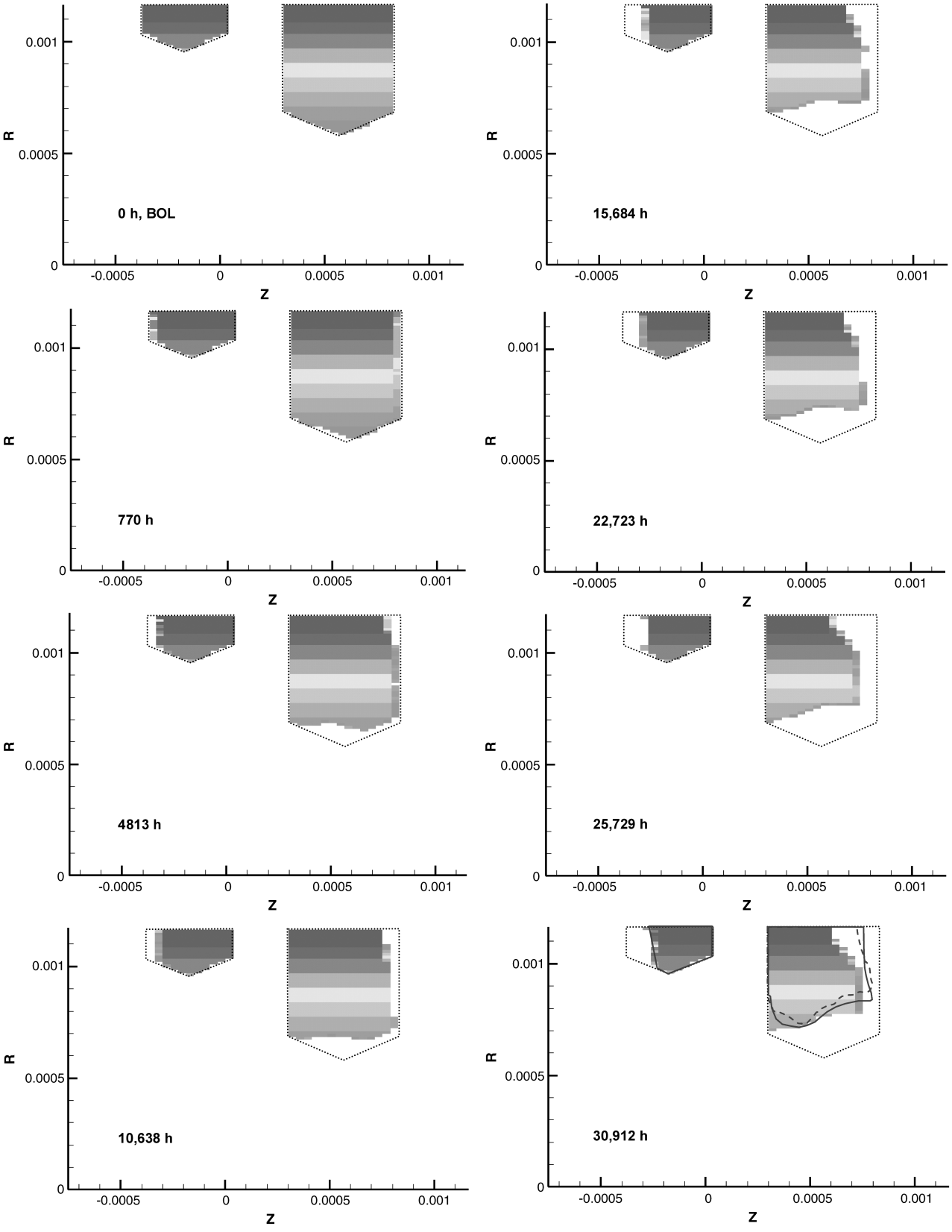

Fig. 8 Progressive time-dependent erosion estimate for ELT using CEX2D-t.

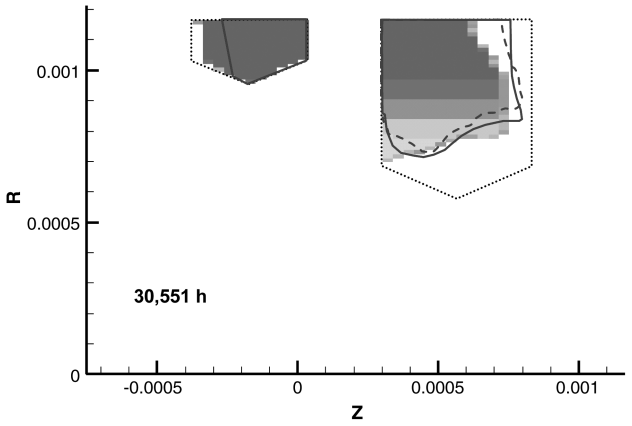

Fig. 9 Final erosion profile for ELT without double ions, $\gamma = 0$.

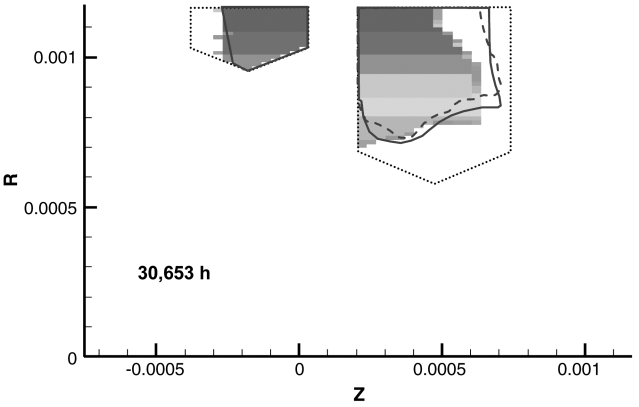

Fig. 10 Final erosion profile for ELT using constant grid gap of 200 μm.

cusp erosion → cylindrical erosion → chamfer erosion

the approximate timeline of which is shown later in Fig. 11. To examine the influence of double ions, the same parameters for the ELT were used, except without double ions (i.e., $\gamma = 0$). The results of this computational sensitivity analysis, shown in Fig. 9, agree with the parametric analysis, in that the doubles will greatly augment upstream screen erosion and will have little effect on the acceleration grid erosion. A similar sensitivity was performed with grid spacing, using constant grid spacings of 200 and 400 μm to compare with the nominal 300 μm spacing. The erosion profiles for the 200 μm spacing from Fig. 10 show that the acceleration grid erosion is very similar to the nominal case. The slightly lower screen erosion is expected, since the smaller 200 μm spacing increases the ion transparency of the grids, thus reducing the upstream plasma density requirement and reducing the ion bombardment rate on the upstream screen grid surface. Figure 11 shows the estimated acceleration hole diameter determined by the code for constant grid gaps of 200, 300, and 400 μm compared against data measured from the ELT. The results for all cases compare well with the experimental data; however, aperture diameters later in the test are smaller, since the model is not predicting the slight upstream chamfering observed in the test. This upstream chamfering is observed for simulations performed for the properties of gridlets at a grid radius of 7 cm, but additional analysis is need to determine what is causing the upstream chamfering.

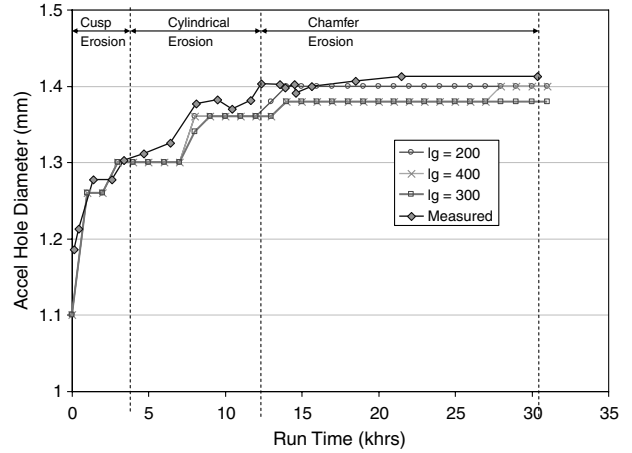

Fig. 11 Acceleration grid center-hole diameter vs time simulations of ELT using CEX2D-t. Results are shown for constant grid gaps (lg) of 200, 300, and 400 μ.

IV. Conclusions

This effort represents a significant step toward using modeling to aid in the prediction of ion thruster performance and life for long-duration missions. The code predicts the major features of grid erosion observed in the LDT and ELT. Double ions greatly increase the screen grid erosion and mitigate the effects of acceleration grid erosion due to CEX ions. The code currently uses only one grid space for an entire run. Results herein show that useful results can be obtained with this limitation; however, the code will benefit greatly from adding the ability to change grid gap as the run progresses, which should improve the prediction of life-limiting mechanisms. The code will also benefit with increased knowledge of inputs (e.g., local double ion content, neutral density, sputter yields, etc.) and experimental erosion measurements (e.g., grid geometry as a function of time), since there is uncertainty in many of the parameters used herein, although such an improvement is not necessary for this initial code validation effort. This 2-D treatment is sufficient to describe general features; however, a 3-D treatment is necessary to capture effects near the radial maximum of the axially symmetric computational boundary, such as pits and grooves erosion of the acceleration grid and chamfering of the upstream surface of the acceleration grid. For additional accuracy, future efforts will also consider redeposition of sputtered grid material and deposition of material sputtered from facility surfaces for comparison with long-duration test validation efforts.

References

[1] Polk, J. E., Anderson, J. R., and Brophy, J. R., "An Overview of the Results from an 8200 Hour Wear Test of the NSTAR Ion Thruster," AIAA Paper 1999-2446, 1999.

[2] Brophy, J. R., "Propellant Throughput Capability of the Dawn Ion Thrusters," Electric Rocket Propulsion Society, Paper IEPC-2007-279, Fairview Park, OH, 2007.

[3] Wirz, R., Katz, I., Goebel, D., and Anderson, J. R., "Electron Backstreaming Determination for Ion Thrusters," AIAA Paper 2008-4732, 2008.

[4] Bond, R. A., and Latham, P. M., "Ion Thruster Extraction Grid Design and Erosion Modeling using Computer Simulation," AIAA Paper 1995-2923, 1995.

[5] Shiraishi, T., Kuninaka, H., Satori, S., and Kuriki, K., "Numerical Simulation of Grid Erosion for Ion Thruster," Electric Rocket Propulsion Society, Paper IEPC-9590, Fairview Park, OH, 1995.

[6] Nakano, M., and Yoshihiro, A., "Ion Thruster Lifetime Estimation and Modeling Using Computer Simulation," Electric Rocket Propulsion Society, Paper IEPC-99-145, Fairview Park, OH, 1999.

[7] Nakano, M., "A Grid Lifetime Model for a 3-Grid Ion Engine," Electric Rocket Propulsion Society, Paper IEPC-01-84, Fairview Park, OH, 2001.

[8] Nakano, M., "Three-Dimensional Simulations of Grid Erosion in Ion Engines," *Vacuum*, Vol. 83, No. 1, 2008, pp. 82–85. doi:10.1016/j.vacuum.2008.03.080

[9] Emhoff, J. W., and Boyd, I. D., "Modeling of Total Thruster Performance for NASA's Evolutionary Xenon Thruster Ion Optics," *Journal of Propulsion and Power*, Vol. 22, No. 4, 2006, pp. 741–748. doi:10.2514/1.18975

[10] Farnell, C. C., Williams, J. D., and Wilbur, P. J., "Numerical Simulation of Ion Thruster Optics," Electric Rocket Propulsion Society, Paper IEPC-2003-073, Fairview Park, OH, 2003.

[11] Brophy, J. R., Katz, I., Polk, J., and Anderson, J. R., "Numerical Simulations of Ion Thruster Accelerator Grid Erosion," AIAA Paper 2002-4261, 2002.

[12] Miller, J. S., Pullins, S. H., Levandier, D. J., and Dressler, R. A., "Xenon Charge Exchange Cross-Sections for Electrostatic Thruster Models," *Journal of Applied Physics*, Vol. 91, No. 3, 2002, pp. 984–991. doi:10.1063/1.1426246

[13] Doerner, R. P., Whyte, D. G., and Goebel, D. M., "Sputtering Yield Measurements During Low Energy Xenon Plasma Bombardment," *Journal of Applied Physics*, Vol. 33, No. 9, May 2003, pp. 5816–5823. doi:10.1063/1.1566474

[14] Stuart, R. V., and Wehner, G. K., "Sputtering Yields at Very Low Bombarding Ion Energies," *Journal of Applied Physics*, Vol. 33, No. 7, 1962, pp. 2345–2352. doi:10.1063/1.1728959

[15] Wirz, R., "Discharge Plasma Processes of Ring-Cusp Ion Thrusters," Ph.D. Dissertation, Aeronautics, California Inst. of Technology, Pasadena, CA, 2005, http://thesis.library.caltech.edu/1974/1/Wirz_Thesis.pdf [retrieved 2010].

[16] Patterson, M. J., Haag, T. W., and Rawlin, V. K., "NASA 30 cm Ion Thruster Development Status," AIAA Paper 1994-2849, 1994.

[17] Diaz, E. M., and Soulas, G. C., "Grid Gap Measurement for an NSTAR Ion Thruster," NASA TM 2006-214249; also Electric Rocket Propulsion Society, Paper IEPC-2005-244, Fairview Park, OH, 2005.

[18] Anderson, J. R., Katz, I., and Goebel, D., "Numerical Simulations of Two-Grid Ion Optics Using a 3-D Code," AIAA Paper 2004-3782, 2004.

A. Gallimore
Associate Editor